DOI: 10.1016/j.talanta.2023.124680

Combining micro- and portable-XRF as a tool for fast identification of virus infections in plants: the case study of ASa-Virus in *Fraxinus ornus* L.

Authors:

Carlo Porfido[1,*], Kira Köpke[2], Ignazio Allegretta[1,3], Martina Bandte[2], Susanne von Bargen[2], Malgorzata Rybak[4], Gerald Falkenberg[5], Tanja Mimmo[6,7], Stefano Cesco[6], Carmen Büttner[2], Roberto Terzano[1]

[1] Department of Soil, Plant and Food Sciences, University of Bari "Aldo Moro", Via Amendola 165/A, 70126, Bari, Italy

[2] Humboldt-Universität zu Berlin, Division Phytomedicine, Berlin, Germany, Lentzeallee 55/57, 14195, Berlin, Germany

[3] Department of Biological and Environmental Sciences and Technologies, University of Salento, via Monteroni 165, 73100, Lecce, Italy

[4] Plant Protection Service Hamburg, Ministry of Economy and Innovation, Free and Hanseatic City of Hamburg, Brennerhof 123, 22113, Hamburg, Germany

[5] Deutsches Elektronen-Synchrotron DESY, Notkestrasse 85, 22607, Hamburg, Germany

[6] Faculty of Science and Technology, Free University of Bolzano, Piazza Universitá 5, 39100, Bolzano, Italy

[7] Competence Centre for Plant Health, Free University of Bolzano, Piazza Universitá 1, 39100, Bolzano, Italy

Corresponding author*: carlo.porfido@uniba.it

Abstract

Plant viruses can affect micro- and macro-nutrients homeostasis in woody plants, with fluctuation of some elements' concentrations at the leaf level as a consequence of the pathogen's activity and/or the plant physiological response to the infection.

Leaves of *Fraxinus ornus* L. (flowering ash) were sampled for three consecutive years in the city of Hamburg (Germany), both from trees showing the typical symptoms of ash shoestring associated virus infection (ASaV+) and healthy ones (ASaV-). Such leaves were analyzed by μ-XRF, using both laboratory and synchrotron X-ray sources. Large differences between infected and healthy leaves were observed: ASaV+ samples showed uneven element distribution and regions of the lamina with severe depletions of P, S, and Ca. Differently, K appeared more concentrated. Thus, 139 leaves from various trees and different years were analyzed with a portable XRF instrument, and K and Ca concentrations were quantified. In general, the K:Ca ratio was always significantly higher in ASaV+ samples. Indeed, this trend was verified for all the samplings over the tree years. We conclude that this parameter has potential in the frame of trendsetting diagnostics and could be used, together with visual symptoms, for a rapid, non-destructive, on-site and cheap indirect ASaV detection.

Keywords: nutrient homeostasis, plant virus, *Fraxinus sp*., climate change trees, fast analysis, ionomics

Introduction

It is known that virus infections of trees can frequently induce the onset of visual leaf symptoms that occur in the form of colour changes, shape changes and/or dieback [1-3]. In many deciduous woody plant species, widespread chlorotic colour changes of the leaves such as mosaic, mottling, line patterns and/or vein yellowing occur, which then often necrotize and can lead to premature leaf drop. Moreover, the leaf shape can also be affected by the virus infections with evident changes such as leaf rolling, curling, or severe narrowing of the leaflets, termed shoestring symptoms.

Similarly to what happens for fruit trees in orchards, viruses can also harm deciduous trees in urban areas and in forests, affecting their nutrient supply, vigor and possibly stand stability (e.g., due to a compromised wood quality). Therefore, also for the citizens' safety, the early detection and a deeper knowledge of plant viruses of urban trees is of primary importance [1,2].

In recent years, previously unknown plant viruses have been identified and remarkably also in urban and forest trees. The development of new high-throughput sequencing (HTS) techniques as detection tools has led this big step forward [4,5]. As such, many viruses have also been linked to long-known diseases in important woody plant species of forest and public green areas [6-11]. Increasingly, viral

pathogens are also being identified that have not previously been associated with disease or that populate deciduous woody plants as mixed infections with other pathogens [12,13]. Particularly in long-lived woody plants, various viruses have been often identified that may accumulate in the host plant during its lifetime [10,13].

Besides HTS, ionomic approaches have lately proved their efficacy in this research field by showing significant correlations between the elemental composition of leaves and plant susceptibility/resistance to pathogens [14,15], as well as between the mineral element concentration and/or distribution at leaf level and the plant infection state [16,17]. Indeed, it is ascertained that viral infections massively interfere with and redirects the metabolism of the host plant and can cause modifications in the homeostasis of macro- and micro-nutrients both at the cell and tissue level. In this respect, it is interesting to note that the concentration of some macro- and micro-nutrients significantly changed when leaves of citrus trees have been exposed to citrus tristeza virus (CTV) for more than 10 years, as compared with those collected from non-virus infected ones [16]. In particular, the concentrations of N, Zn, Mg and Fe increased, while the concentration of K decreased in CTV-infected leaves. Furthermore, in alfalfa plants infected by alfalfa mosaic virus (AMV) a marked decrease of P, Fe, Cu, Zn, and Mn concentration has been recorded, while the K levels were not affected by the virus infection [18].

The analysis of macro- and micro-nutrients accumulated in plant tissues is commonly performed, after acid digestion of the plant sample, by atomic spectroscopy analytical techniques such as atomic absorption spectroscopy (AAS), inductively coupled plasma optical emission spectrometry (ICP-OES) and/or inductively coupled plasma mass spectrometry (ICP-MS) [19]. In this respect, it is important to underline that all these analytical techniques are characterized by the complete destruction of the plant sample to be analyzed.

Along with these, X-ray fluorescence (XRF) techniques, either using laboratory X-ray sources or synchrotron radiation (SR), have gained increasing popularity in the last decades to study the elemental composition of different vegetal matrices [20-22]. In fact, such XRF techniques offer various advantages compared to traditional analytical methods, among which multi-element analysis capability, the possibility to analyze directly solid samples without digestion (usually after simple and time-saving sample preparation procedures), and the availability of portable XRF instruments (P-XRF), which can be very appealing for field-applications [23]. Furthermore, aside bulk analysis, XRF can be exploited, using micro-focusing optics (μ-XRF), for the non-destructive elemental mapping of plant tissues, e.g., leaves or roots [17,24,25], with micrometric resolution. Since leaves are particularly sensitive to viruses and other biotic stresses, often showing localized changes in elements concentrations and/or distributions at the mm/μm scale [26,27], μ-XRF spectrometry hence

represents an effective tool to better characterize the host-pathogen interactions affecting the dynamics of nutrients' distribution at the leaf level.

This paper presents the results of a three-year investigation (2019-2021) on ash shoestring-associated virus (ASaV) infected flowering ash (*Fraxinus ornus* L.) trees planted in the city of Hamburg (Germany). Flowering ash is an important urban woody plant species in the future city green and considered as a "potential climate tree species" [28,29]. The species is characterized by temperature tolerance associated with prolonged dry periods in urban areas, while bringing a necessary frost tolerance. In addition, they are insensitive to the fungal pathogen of ash shoot dieback and are therefore preferentially planted in street and urban locations to replace the susceptible common ash (*F. excelsior*). As with most other deciduous species, viral diseases of ash trees present a special challenge because they cannot be controlled curatively.

In Hamburg, many of the 166 flowering ash trees planted from 2016 as climate tree species, showed the typical ASaV symptoms, *i.e.*, leaf deformation, shoestrings and spotting [30]. For this study, starting from 2019, leaf samples have been collected from both symptomatic and not symptomatic trees and the infection status verified through Reverse Transcriptase Polymerase Chain Reaction (RT-PCR). After that, laboratory and synchrotron μ-XRF, and P-XRF were jointly used with the aim of investigating whether ASaV infection interfere with mineral elements accumulation and distribution at the leaf level (namely the plant organ in which the symptoms appear) and, *vice versa*, whether such modifications in elements homeostasis in symptomatic leaves can be used for the ASaV infection diagnosis in *F. ornus*.

Materials and Methods

Sampling site

The Hamburg metropolitan region is located in the border area between the cold polar regions and the warm subtropics. Summers are moderately warm and humid; winters are mild due to the influence of the North Atlantic Oscillation [31]. However, weather records showed significant changes over the last 100 years with a trend toward drier summer months and a significant increase in precipitation in the fall and winter [32].

The annual mean air temperature for Hamburg is 9.4 °C, the annual mean sum of precipitation 796 mm per year, and the mean annual sum of sunshine duration 1584 h. Precipitation was in the range between 2019 and 2021 with 752, 668, and 725 mm of precipitation, respectively [33,34].

The sampling site is located in Haffkruger Weg (53°36'41.4"N 10°08'58.7"E), Hamburg (Germany), where single-family houses with gardens are predominantly at the stand. Flowering ash trees were

planted (2016-2018) on site in a tree nursery substrate along the green strip between the coble stone street and the sidewalk (Fig. 1A). The local soil can be classified as cambisol [35].

Sampling, sample preparation and molecular analyses for virus identification

An overview of the sampling of flowering ash leaves is presented in Table S1. In June 2019, leaves were taken from the upper part of the canopy of one flowering ash (H1) without virus-suspicious symptoms, and a second tree (VI1) showing typical ASaV symptoms (Fig. 1B and Fig. 1C). ASaV infection was then confirmed by RT-PCR (see below). The same two trees and one additional virus infected ash (VI2) were sampled in 2020 two times (August and September). In 2021, those three trees were sampled in June, July and August. At the second and third sampling in 2021, two additional healthy trees (H2 and H3) were included in the study to increase the statistics for the analyses performed with P-XRF (Tab. S1). Three leaves per tree were taken from both infected and healthy ashes in each sampling period. Leaves from infected trees showed typical ASaV symptoms. ASaV infection was then confirmed by RT-PCR (see below). All samples were handled with gloves and stored in plastic bags, as a humid chamber, and transported to the laboratory in a cooling box.

Once in the laboratory, leaves were washed with deionized water, then leaflets from each leaf were separated and prepared accordingly to the analysis to which they were intended for. A scheme of leaflet selection is reported in Fig. S1. Leaflets for RT-PCR were stored at -80 °C, then ASaV detection was performed by RT-PCR targeting RNA3 and RNA4 of the virus in combination with Sanger sequencing as described by Gaskin *et al.* [30]. Leaflets for XRF analyses were prepared by inserting them between two circles of filter paper and keeping them pressed within a Petri dish, as described in Terzano *et al.* [24]. Thereafter, the leaves were quickly frozen by pouring over the petri dish liquid nitrogen, kept on dry ice and finally freeze-dried under vacuum (Christ Gamma 1-16, Martin Christ Gefriertrocknungsanlagen GmbH, Osterode am Harz, Germany). Freeze dried samples were stored in plastic bags with paper bags filled with Celite pearls to prevent rehydration.

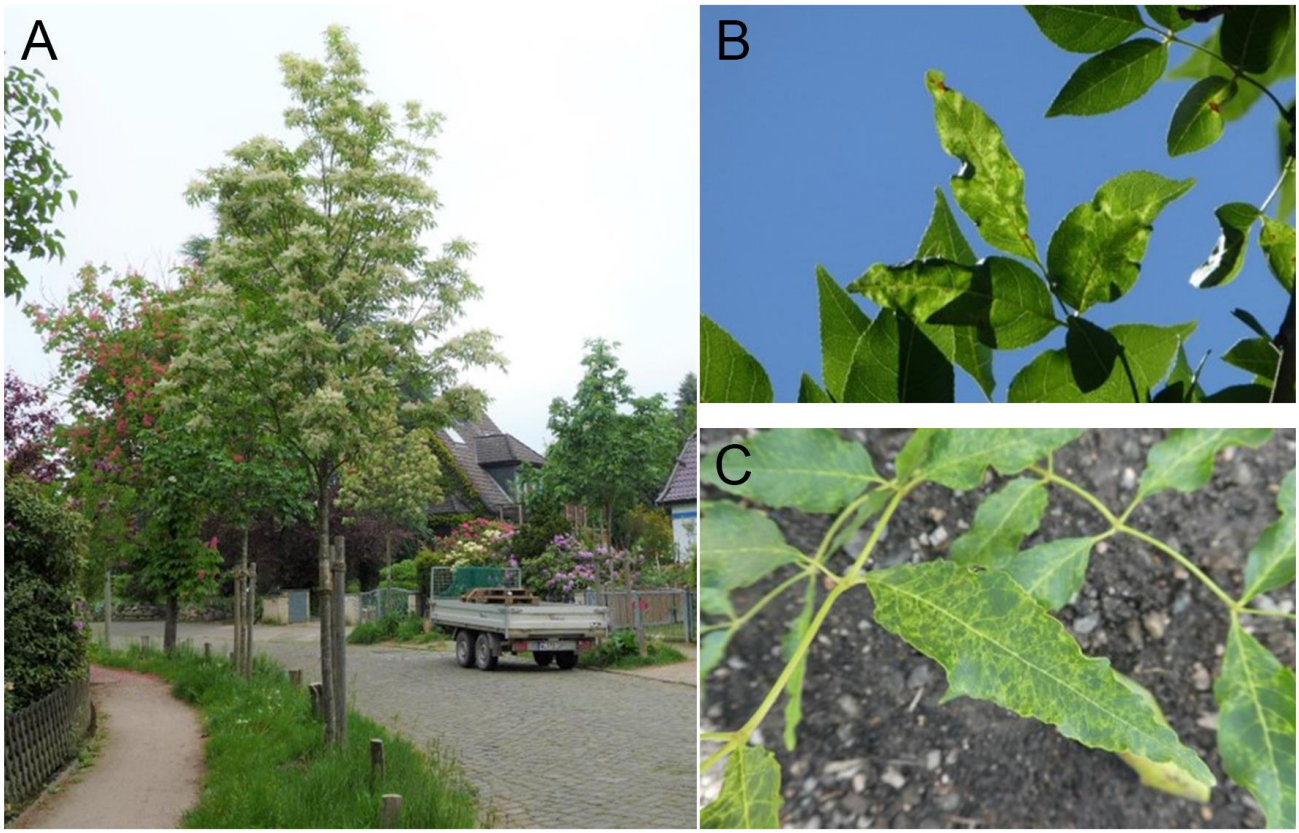

Fig. 1: (A) Flowering ash at sampling site Haffkruger Weg, Hamburg, May 2019; (B) ASaV typical symptoms in tree`s crown; (C) ASaV infected leaflets.

153

154 *X-ray fluorescence analyses*

155 A benchtop µ-XRF spectrometer (M4 Tornado, Bruker Nano GmbH, Berlin, Germany) was used to
156 collect micro-focused X-ray fluorescence elemental maps of representative areas of the upper surface
157 of at least one leaflet per flowering ash tree in every sampling episode (Tab. S1). The µ-XRF
158 instrument is equipped with a micro-focus Rh X-ray source (50 kV, 600 µA), a polycapillary X-ray
159 optics with a spot-size of 25 µm and two XFlash™ energy dispersive silicon drift detectors (SDD)
160 with 30 mm^2 sensitive area and an energy resolution of 140 eV @ Mn Kα. The specific set up of the
161 two detectors, placed at opposite sites compared to the X-ray optics, reduces shadowing effects in the
162 elemental maps and improves the signal-to-noise ratio (S/N). For each leaflet, a rectangular area (16
163 x 10 mm, or less for smaller leaflets) was selected for analysis approximately at the middle-right side
164 of the leaflet (including the midrib) (Fig. S2, blu rectangle). All µ-XRF maps were acquired under
165 near-vacuum conditions (20 mbar) using 25 µm pixel size and 10 ms acquisition pixel time. The
166 scanning was repeated 5 times for each sample and the relative spectra averaged in order to increase
167 S/N. Micro-XRF distribution maps were obtained with the ESPRIT software (Bruker Nano GmbH,
168 Berlin, Germany, version 1.3.0.3273) and further processed by PyMca 5.1.3 [36] and Datamuncher
169 [37] software.

In addition to the μ-XRF analyses carried out using a laboratory benchtop spectrometer, higher resolution and more sensitive analyses were also performed on few selected leaflets (July 2020 sampling) at the P06 beamline of the synchrotron PETRA III of the Deutsches Elektronen-Synchrotron (DESY) in Hamburg (Germany). The X-ray beam was set at 15 keV and focused with a Kirkpatrick-Baez mirror system obtaining a spot size of 300 x 500 nm (height x length). Scans were performed on areas of 2 x 2 mm (Fig. S2, green square) in continuous mode using a step size of 10 μm and a dwell time of 100 ms. The fluorescence signal was collected by an ARDESIA-16 detector placed at 90° with respect to the incident beam [38]. The datasets were then fitted using the "Batch Fitting" tool of PyMCA [36].

A large set of ASaV+ (VI, n=70) and ASaV- leaflets (H, n=69) collected from 2019 to 2021 was analyzed for K and Ca concentration (expressed as μg cm^{-2}) using a portable energy dispersive XRF spectrometer (P-XRF, NITON™ XL3t, Thermo Scientific, Waltham, USA). This instrument is equipped with an Ag collimator source (spot size ca. 6 mm) operating at 50 kV and 40 μA and a large area SDD detector (160 eV resolution @ Mn Kα). Four points per leaflet (apex – near petiole – middle left – middle right, Fig. S2, red circles) were analyzed (30 s live time per point) for each sample and the results averaged. Quantitative data were obtained using the Thermo-NITON instrument proprietary software (NDTR version 6.5.2) in "Standard filter mode". This method has been originally developed for the analysis of cellulose filter papers. The matrix of the samples was assumed to be uniformly constituted of cellulose [24] and the leaf thickness is comparable to that of filter paper. Cellulose filter standards containing 100 and 200 μg cm^{-2} of Ca and K were in-house prepared by adding calculated amounts of KNO_3 and $Ca(NO_3)_2$ (>99%, Sigma Aldrich, St. Louise, USA) solutions to Whatman N°5 filter paper (Maidstone, UK) and used to check the instrument accuracy. Specifically, the 100 and 200 μg cm^{-2} Ca and K filter standards were prepared by homogenously adding dropwise 2 ml or 4 ml, respectively, of a 1 mg ml^{-1} Ca or K solution to a 20 cm^2 (5 cm × 4 cm) piece of filter paper and letting it dry on a heating plate at 40°C under a laminar flow hood.

Statistics

K:Ca ratios are expressed as means (± SD). Student's t-test ($p<0.05$) was used to compare the mean K:Ca ratios (healthy *vs* infected). One-way ANOVA was applied on the data acquired on the leaves sampled within the same period and a two-way ANOVA was performed on the whole dataset considering the tree and the sampling period as parameters. In both cases, a $p<0.05$ was considered and the nonparametric Tukey's test was used to group the samples. Finally, samples were classified using linear discriminant analysis (LDA) as a supervised classification method. The accuracy of the classification was estimated by the ratio between the number of correct classified samples and the

total number of analyzed points, in percentage. All the statistical analysis and the classification were carried out using Minitab 18 (Minitab, State College, PA, USA).

Results

Visual symptoms and molecular virus identification

Leaves collected from flowering ash trees VI1 and VI2 showed mottle, chlorotic lines and spots, and ringspots in some leaf areas. Further, leaf deformations like curling and shoestring symptoms occurred in various intensity during all the three investigated vegetation periods (Fig. 1B and Fig. 1C). Leaf symptoms persisted on both trees throughout the vegetation periods. In 2021, the symptom expression on leaves appeared to be weaker than in the previous two vegetation periods. We could not observe such symptoms in the flowering ash trees scored as healthy (H1-H3) in any of the leaves of their canopies.

ASaV was detected in all analysed leaflets from the sampled flowering ash trees VI1 and VI2 and not in any sample from healthy trees (H1-H3), during the whole period of investigation (2019-2021).

µ-XRF analyses

Fig. 2A shows grey-scale element distribution maps obtained after combining the µ-XRF database of a healthy (ASaV-) and an ASaV+ leaflet with Datamuncher software. This data visualization allows comparing the elemental distribution maps both qualitatively (i.e., pattern of nutrients' distribution) and semi-quantitatively, since the same intensity scale was used for both leaflets (pixels with higher element concentration are brighter while lower concentrations appear darker). In particular, Fig. 2A shows P, S, K, Ca, Mn, Fe and Zn distribution maps. These are the main elements revealed by µ-XRF analysis, grouped as macronutrients (left column) and micronutrients (right column). Due to the very low concentration of the latter, the contrast of Mn, Fe and Zn maps was enhanced to make them more easily visible (as evident from the different greyscale).

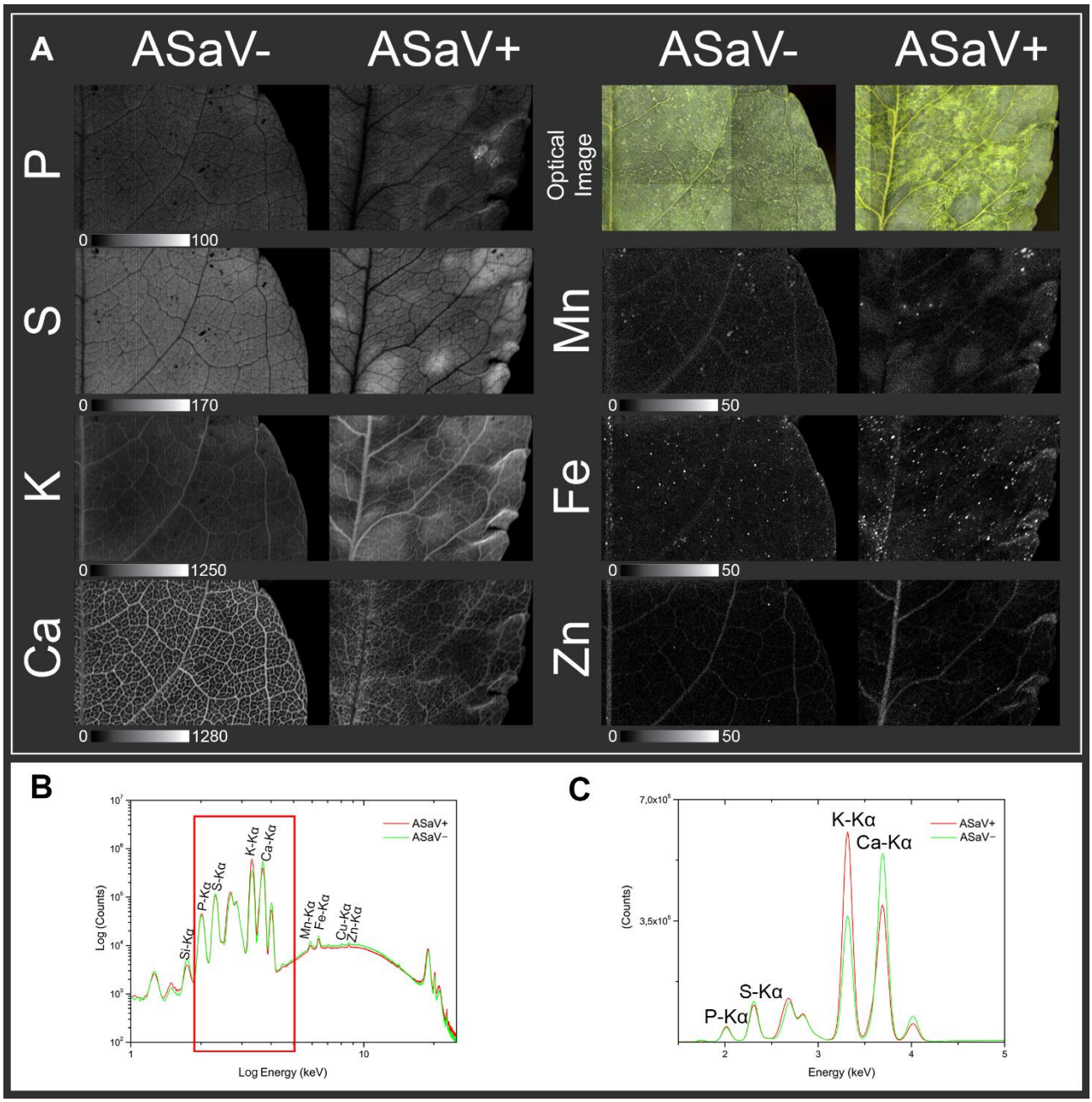

Fig. 2: (A) Comparison of laboratory µ-XRF elemental maps (P, S, K, Ca, Fe, Mn, Zn) of a leaflet from healthy (AsaV-) flowering ash (H1) *vs* a leaflet of an ash shoestring-associated virus infected (ASaV+) tree (VI1); grey scale. Intensity scale bars (counts/s) are tuned element-by-element allowing the direct comparison of element concentration between ASaV- and ASaV+ leaflets. Bottom panel (B) µ-XRF (Log-scaled) sum-spectra comparison of a square region of interest (200x200 pixels) of the leaflets; (C) zoom of a selected energy region of the spectrum (outlined in red in B) showing the macronutrients (P, S, K and Ca) fluorescent signals (linear scale).

Looking at the macronutrients (P, S, K, Ca) maps (Fig. 2A), it is evident that their distribution in the healthy leaflet is regular, with no significant changes over the entire analysed area. Calcium is more

concentrated within the veins (including secondary veins, tertiary veins, etc.); K is more abundant in the veins than within the interveinal lamina area, whereas P and S are distributed almost homogeneously in the leaf lamina and less concentrated in the veins. Such distribution patterns are markedly different if the infected leaflet is considered (ASaV+, Fig. 2A). Phosphorus, S, K and Ca spatial distribution indeed appears strongly inhomogeneous when compared to the corresponding healthy tissues, especially within the interveinal lamina areas.

With respect to the micronutrients contents and their distribution within the leaf (Fig. 2A), elemental maps are noisier (due to lower concentrations), therefore, differences are more difficult to detect. In the infected leaflet, Mn appears more concentrated in the lamina whereas it is more concentrated in the primary and secondary veins of the healthy one. Finally, Fe and Zn distributions appear rather similar. To have a semi-quantitative estimation of these observations, sum spectra of equivalent selected areas (i.e., 200 x 200 pixels) were compared for the two leaflets (Fig. 2B). The healthy leaflet showed higher Ca concentrations than the virus infected one, while K concentration was clearly lower (Fig. 2C). Differently, despite the different distribution observed in the elemental maps of healthy and virus infected samples (Fig. 2A), P and S total concentrations did not significantly change in the observed samples (**Errore. L'origine riferimento non è stata trovata.**2B and Fig. 2C).

All these results can be considered representative of the results generally obtained for the leaflets collected over the whole period of investigation, as also shown in Fig. 3.

Fig. 3 shows the distribution of macronutrients (P, S, K and Ca) of a healthy and a virus infected *Fraxinus ornus* L. leaflet per each year of sampling. In addition, multi-element maps (overlay of P, S, K and Ca maps) are presented in the last column of Fig. 3. Regardless of the sampling year, healthy leaflets show always very similar macronutrient distributions, as it can be noticed both by mono- and multi-elemental maps. Looking at multi-elemental maps, the veins' network appears of a lighter colour: this is due to the higher concentration of K and Ca (orange + green). Besides, leaf lamina is pinkish due to the overlapping of P and S signals (blue + red). Moreover, as observed also in Fig. 2A, healthy leaflets always show a regular elemental distribution, not changing over the whole leaf area analysed. Differently, the multi-element maps of virus infected leaflets show uneven element distributions if compared to the corresponding healthy leaves. Indeed, infected leaflets exhibit "patchy" distribution patterns. In general, it seems that a change in S, P, Ca and K distribution over the leaf tissues is associated to ASaV infection. These data also would suggest a correlation between the degree of such inhomogeneity and the severity level of the infection symptoms visually observable at the leaflet's surface (first column of Fig. 3).

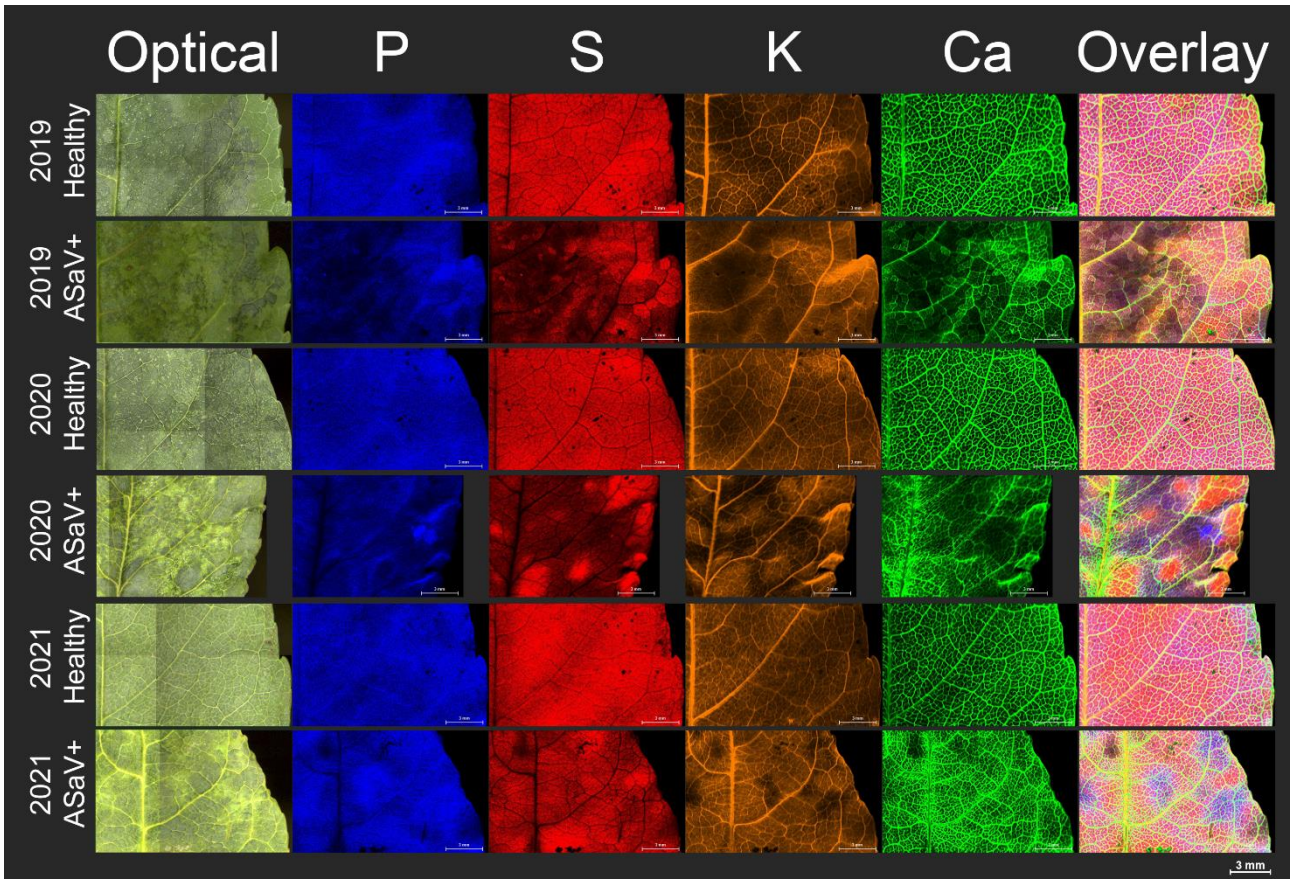

Fig. 3: Optical image and laboratory μ-XRF elemental distribution maps (P, S, K, Ca and their overlay). For each sampling year a healthy (ASaV-) and an infected (ASaV+) leaflet is shown.

SR μ-XRF analyses

Elemental distribution maps of K, Ca, Mn, Fe, Cu and Zn were collected at higher resolution in both healthy and virus infected samples (July 2020) by synchrotron μ-XRF (Fig. 4) in a square area right close to the leaf midrib (Fig. S2), including the initial stretch of a secondary vein. In this case, brighter colours correspond to relatively higher concentrations. The data acquired generally confirm, at a smaller but more detailed scale, what was previously observed with benchtop μ-XRF. Indeed, subtler details can be now detected, and micronutrients (Mn, Fe, Zn) distribution maps are better visualized, including Cu distribution that could not be mapped with laboratory μ-XRF. In more detail, K concentration is higher in the infected sample, especially within the interveinal lamina areas, while Ca appears more concentrated in the healthy sample, being distributed mainly in the vascular regions. As for the other elements, Mn is more concentrated in the interveinal lamina region of the infected leaflet, where also some areas with higher Fe concentration have been observed. The distribution of Cu is very similar in healthy and infected leaflets, while Zn concentration seems to be lower in the healthy than in the infected leaflet.

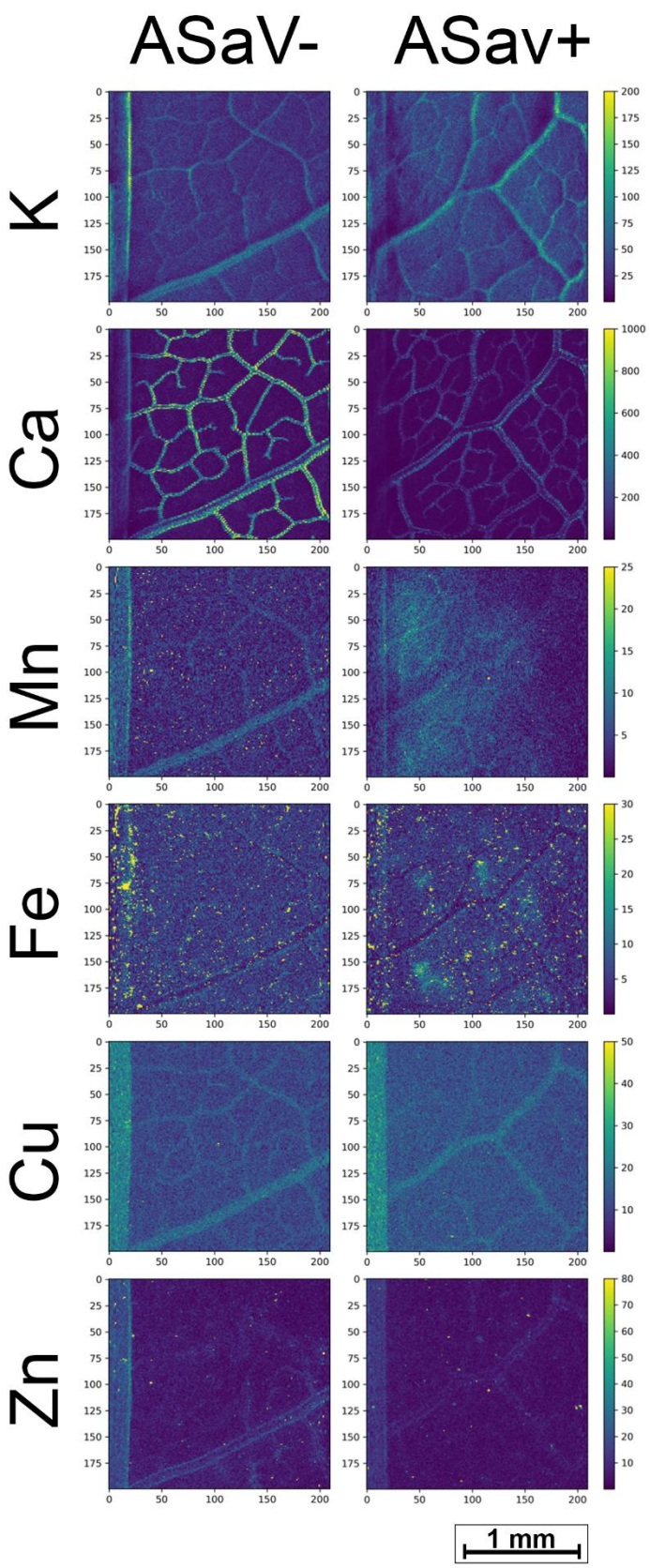

Fig. 4: Synchrotron μ-XRF distribution maps of K, Ca, Mn, Fe, Cu and Zn. Intensity bars (counts/s) are tuned element-by-element allowing the direct comparison of element concentration between healthy (ASaV-) and infected leaflets (ASaV+).

281

Looking at the secondary veins, it is also possible to distinguish higher elemental concentrations of Ca, Fe and Zn in the external part of the veins (where xylem vessels are located), while the central region (where the phloem vessels are located), appears almost depleted of these elements. Manganese, Fe, and Zn maps show also randomly distributed spots of high intensity, probably attributable to exogenous materials such as dust particles not completely removed after leaf washing, which partially affect the quality of the distribution images, especially for Fe [24]. Overall, albeit the higher resolution and the higher sensitivity obtained when using SR micro-XRF, laboratory μ-XRF results allowed to better visualize the redistribution of the elements after the ASaV infection (i.e., the "patchy" patterns described above) both because of the larger area irradiated and the mapping of S and P (which could not be obtained at synchrotron due to the lack of a vacuum chamber). Furthermore, even if SR also unveiled variations in the distribution of trace elements such as Mn and Zn, these two elements were generally in concentrations below the limits of quantification of portable XRF instruments. Therefore, as described in the next section, our attention was addressed only to major elements such as K and Ca, whose concentration could be easily and expeditiously determined by P-XRF and therefore suitable for screening a much larger set of samples.

P-XRF analyses

Both laboratory and SR μ-XRF analyses revealed changes in element concentration and distribution comparing healthy and virus infected samples. In particular, significant differences were observed for the two macronutrients K and Ca. Based on these observations, we hypothesised that such two elements could be used, e.g., together with visual symptoms, as an indicator of ASaV infection. For this purpose, we used a portable XRF instrument (easily manageable in the field and allowing fast analyses – 30 s per point) to analyze Ca and K concentration of a large set of healthy (n=69) and infected (n=70) leaflets covering the entire three years sampling period (2019-21). It is worth specifying that, among infected leaves, not all the leaflets showed acute symptoms, some leaflets even not showing clear visual symptoms.

In Fig. 5A and Fig. 5B, the scatterplots show the correlations between K and Ca concentrations in the leaflets of the H1 and VI1 trees, respectively, as determined by means of P-XRF over the three years experimental period. In leaflets of H1 (Fig. 5A), Ca concentration generally ranged from 70 to 200 μg cm^{-2} while K was comprised between 110 and 160 μg cm^{-2}. Lower Ca concentrations were found in early summer samples (e.g., H1-Jun 19 and H1-Jun 21); thereafter its concentration increased during the summer, reaching a maximum in August and September. Conversely, K concentration did not significantly change nor showed a particular trend during the vegetative period. Differently from the healthy leaflets (H1), in the virus infected leaflets (VI1) K concentration increased concomitantly

with Ca concentration (Fig. 5B), with a correlation coefficient R^2=0.78. On average, K concentration was generally higher in the virus infected leaflets (VI1) compared to the healthy ones (H1) while Ca was less concentrated than in H1, never exceeding 140 µg cm^{-2}. Scatterplot in Fig. 5C shows the whole P-XRF dataset (n=139). Red (infected leaflets) and green (healthy leaflets) points clearly cluster separately in certain regions of the graph, while in fewer cases they appear mixed in the central part of the graph. Looking at these data, the following considerations can be done, regardless of the year and/or month of sampling and the tree considered: i) except for two "false positives", higher K concentrations (e.g. >160 µg cm^{-2}) are always associated to ASaV infected samples; ii) for K<160 µg cm^{-2}, samples are always healthy at the higher Ca values (e.g. >100 µg cm^{-2}); iii) samples with lower Ca concentration (e.g. <60 µg cm^{-2}) are always ASaV infected; iv) in the range 60<Ca<100 µg cm^{-2} and 110<K<160 µg cm^{-2} both healthy and ASaV infected leaflet samples can be found. However, when considering the K:Ca ratio, this value is in the great majority of cases higher in infected leaflets compared to healthy ones, as shown by the graph shown in Fig. 5D. Indeed, the average K:Ca ratio for all the tested leaflets was 2.0 ± 0.7 for infected samples (n=70) and 1.2 ± 0.4 (n=69) for healthy samples. Such values are significantly different at p<0.05 (*t*-test). Moreover, the graph in Fig. 5E shows that in each sampling period over the three years, the K:Ca ratio is always higher for infected leaflets (orange and red dots) if compared with healthy ones (green dots).

The application of the one-way ANOVA coupled with Tukey's test on the K:Ca data of healthy and infected leaflets sampled in the same period demonstrates that the two groups are statistically different for a value of $p < 0.05$ (Table 1). Two-way ANOVA coupled with Tukey's test was applied on the whole dataset considering the tree and the sampling period as parameters. It is evident that the samples are divided into two groups which have statistically different K:Ca values and which correspond to the healthy trees (trees H1, H2 and H3) and virus-infected trees (VI1 and VI2) despite the sampling period (Table 1). The data acquired in different sampling periods are generally statistically different one from the other (considering the year of sampling). The only exception are the data of June 2019 which are statistically similar to the ones of the other sampling periods. Based on these results, linear discriminant analysis (LDA) was applied on the dataset using the concentration (µg cm^{-2}) of K and Ca as variables (Table 2). Finally, an overall accuracy of 86.3% was obtained in the classification of healthy and infected plants (120 correctly classified leaves on a total of 139). In particular, a 90.0% of accuracy was obtained in the identification of infected plants demonstrating the good diagnostic capabilities of these two elements in the identification of the status of *Fraxinus* plants. Moreover, these results also demonstrate the potentiality of this approach for the recognition of early stage of infection; in fact, as mentioned before, many leaflets analyzed through P-XRF for K and Ca concentration did not show clear visual symptoms of infections.

Table 1: One-way and two-way ANOVA coupled with Tukey's test on the K:Ca ratio calculated for the trees H1, H2, H3, VI1 and VI2 along all the sampling periods ($p < 0.05$). For the Tukey's test the letters were given using alphabetic order from the highest to the lowest value.

Sample	Status	Month	Year	K:Ca		One-way ANOVA	Two-way ANOVA	
				m	s		Tree	Period
H1	Healthy	June	2019	1.63	0.17	B	B	ABC
VI1	Infected	June	2019	1.94	0.09	A	A	ABC
H1	Healthy	August	2020	0.88	0.15	B	B	CD
VI1	Infected	August	2020	1.67	0.23	A	A	CD
VI2	Infected	August	2020	1.71	0.26	A	A	CD
H1	Healthy	September	2020	0.77	0.13	C	B	D
VI1	Infected	September	2020	1.69	0.20	A	A	D
VI2	Infected	September	2020	1.43	0.20	B	A	D
H1	Healthy	June	2021	1.75	0.21	A	B	A
VI1	Infected	June	2021	2.29	0.16	AB	A	A
VI2	Infected	June	2021	3.15	1.33	B	A	A
H1	Healthy	July	2021	1.66	0.10	AB	B	B
H2	Healthy	July	2021	1.54	0.04	AB	B	B
H3	Healthy	July	2021	1.19	0.13	B	B	B
VI1	Infected	July	2021	1.97	0.12	A	A	B
VI2	Infected	July	2021	2.40	0.80	A	A	B
H1	Healthy	August	2021	1.37	0.11	B	B	B
H2	Healthy	August	2021	1.56	0.34	AB	B	B
H3	Healthy	August	2021	1.09	0.29	B	B	B
VI1	Infected	August	2021	2.08	0.40	A	A	B
VI2	Infected	August	2021	2.02	0.60	A	A	B

Table 2: Classification of leaves status with LDA using K and Ca concentrations as variables.

	K				Ca				LDA		
	m	s	Min	Max	m	s	Min	Max	Real	Prediction		Accuracy of classification
	[µg*cm^{-2}]									Correct	Wrong	%
Healthy	135	19	102	208	118	37	66	198	69	57	12	82.6
Infected	171	29	81	226	91	29	30	149	70	63	7	90.0
Total									139	120	29	86.3

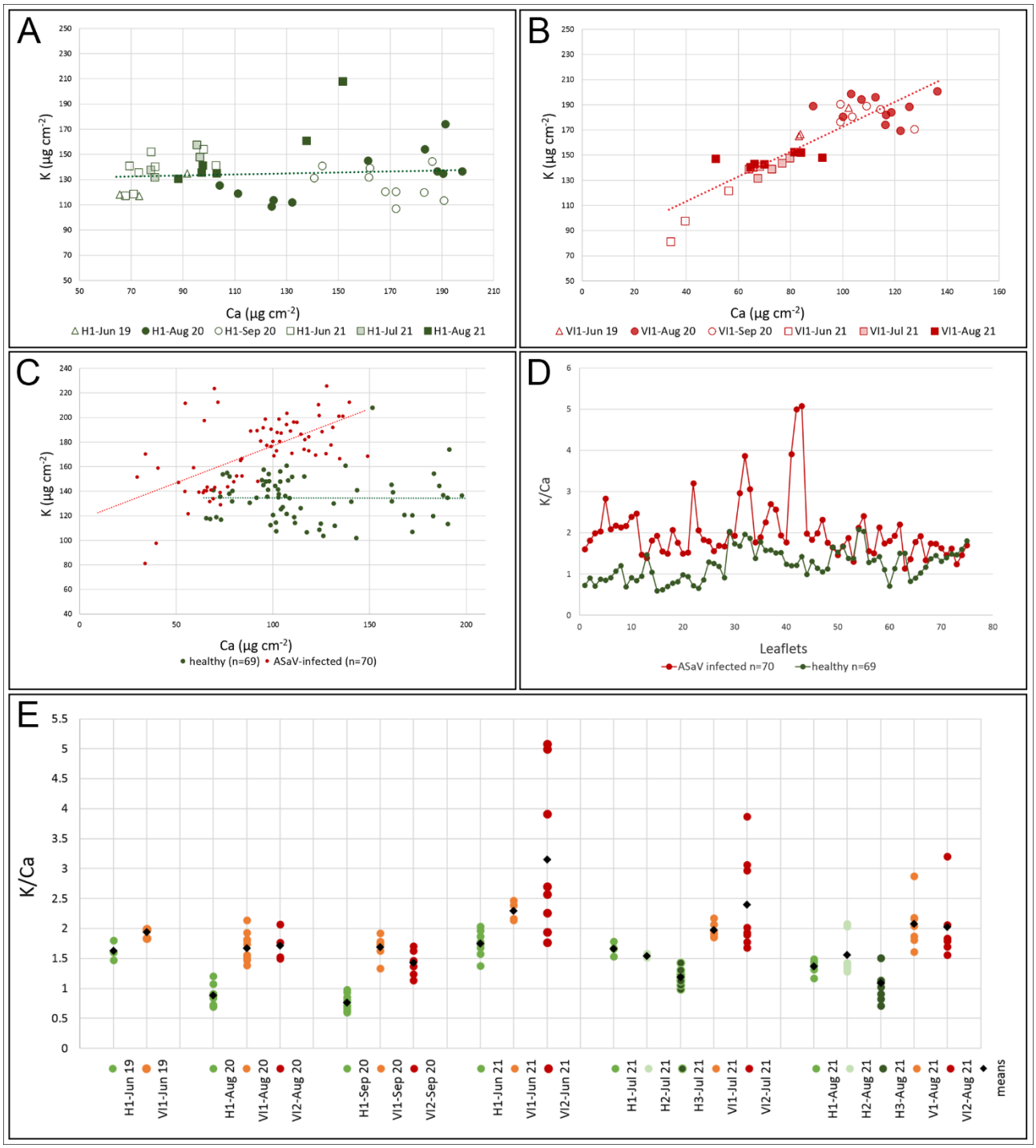

Fig. 5: (A) Ca vs K concentration for the healthy tree H1 - triangle: 2019; circle: 2020; square: 2021; (B) Ca vs K concentration in the virus infected tree VI1 - triangle: 2019; circle: 2020; square: 2021; (C) scatterplot of the 139 analyzed leaflets (green points: ASaV-, n=69; red points: ASaV+, n=70); (D) comparison of K:Ca ratio over the 139 leaflets; (E) overview of K:Ca ratio over the three years sampling.

356

357 **Discussion**

In the present work leaves of *Fraxinus ornus* L. trees grown in the Hamburg city (Germany) have been analysed over the course of three years. Some of these plants showed evident symptoms of ash shoestring-associated virus (ASaV) infection representing a risk not only for the survival of the plant itself but also for its structural stability with possible implications for the safety of residents and their assets. The purpose of the present work was to evaluate the involvement of phenomena associated with nutrients' homeostasis in the leaf (accumulation and distribution within the blade) in the development of the visible symptoms of the infection *via* μ-XRF spectroscopy. These pieces of information are also crucial to evaluate the applicability of portable energy dispersive XRF spectrometers for an early, in-situ/on-site fast and non-destructive detection of the infection directly in the field. Due to these features, such a methodology would present undoubted advantages for a prompt management of the pathology evolution in the area and of the related risks.

The results reported in this work show a clear uneven nutrients' distribution in blades of infected leaves revealing evident symptoms of the ASaV pathology. This phenomenon was particularly noticeable in the case of Ca and K. In fact, while the concentration of the former was decidedly contracted by the infection, that of K increased significantly with the pathology development.

With respect to Ca, it is well known that this nutrient is an essential element for plant's nutrition and it is non-toxic even at high concentrations [39]. In normal growth conditions, Ca concentration in shoots varies from 0.1 to 5 % dry weight. This element accomplishes several functions at the cellular scale, playing both a structural and signaling key role [39-41]. As a divalent cation, Ca^{2+} is involved in membrane stabilization and cell wall strengthening and contributes to osmotic homeostasis within vacuoles and acts as secondary messenger for many signals [39,42]. Differently of K^{+}, Ca^{2+} is xylem but not phloem mobile [39]. Consequently, since this macro-nutrient cannot be re-translocated, Ca accumulation in leaf tissues is definitely xylem-dependent and occurs over time [43]. In fact, it has been observed that Ca concentration is higher in older leaves than in younger ones [43,44]. For instance, Kerton *et al*. [43], while investigating Ca delivery to the leaves of *Coriandrum sativum*, found that Ca concentration in leaves increased significantly between days 5 and 28 of their experiment. On the contrary, K concentration did not change over this period. These findings agree with those reported in Fig. 5A, where an increment of Ca but not of K is observed in the healthy *Fraxinus* leaflets, moving from late spring to early autumn. However, as shown in Fig. 5B and Fig. 5C, the situation is completely different when the ASaV infected leaflets are considered. In fact, in this latter case, while the Ca concentration is on average lower than that measured in the healthy leaves, a clear positive correlation between Ca and K appears evident, with a general increase in K concentration. Looking at the Ca distribution maps in Fig. 2, the general decrease in Ca concentration in infected leaflets is mainly ascribable to large (also darker) regions of the lamina characterized by

392 severe depletions of Ca, S and P. Despite the undoubted clarity of these details in the maps, these
393 evidences are not sufficient to ascertain whether the lower Ca concentration is mainly due to nutrient
394 leakage from the depleted (infected) areas (e.g., caused by the virus infection) or to a lower rate of
395 Ca allocation in those symptomatic regions of the leaf. Concerning this latter hypothesis, it is well
396 known that a virus infection can affect the level of leaf transpiration in the infected areas [45,46], thus
397 being able to have an impact in the levels of the Ca xylem flow towards the sinks of the plant (leaves
398 included). In this regard it is interesting to note that the higher Ca signal recorded in the leaf regions
399 of infected samples but visually not damaged by the infection (and therefore with a transpiration
400 process still almost completely functional – Fig. 2) seems to corroborate this hypothesis. Moreover,
401 it should be emphasized that an increase (pathogen attack-induced) in the cytoplasmic Ca
402 concentration, which in turn acts as a second messenger triggering a number of downstream events,
403 has been yet described in the very early stages of the pathology onset [47]. Furthermore, the
404 involvement of Ca channels in the early defence signals has been also reported [48,49]. Anyhow, it
405 is worth to highlight that the Ca concentration in infected leaves are always lower than in the same
406 blade regions of not infected ones. This phenomenon can be noticed from the lower intensity of the
407 Ca fluorescent signal in the leaves vascular system (Fig. 2A). From a more general point of view, the
408 overall lower availability of Ca in infected leaves with or without symptoms can represent an
409 undoubted issue when the role of this nutrient in the early defence signalling process against potential
410 invaders of the plant cell is considered [50].
411 With respect to K, from a general point of view it represents the most abundant cation in the cytosol;
412 it is not metabolized, highly mobile at all levels in plants, and can usually reach concentration values
413 in the shoot up to 6% of the dry weight of the biomass [39]. It is well known that several biological
414 processes are tightly dependent on this cation, such as metabolic enzymes, photosynthesis and long-
415 distance transport [50]. Results here reported show a clear increase of the K concentration in the
416 infected leaves presenting the typical symptoms of the infection (Fig. 5B). In this respect, it should
417 be highlighted that a clear correlation between availability of K in the growth medium and resistance
418 to the pathogen by the plant has been widely demonstrated, although not always positive [50]. It is
419 interesting to note that recently an enhancement of the virus resistance in rice plants linked to an
420 overexpression of *OsHAK5* potassium transporter has been described [51], highlighting once again
421 the relevance of the homeostasis processes of K in the expression of the resistance trait. Therefore,
422 with respect to the data here presented, a variation of the K contents associated also with a different
423 distribution within the infected leaf appears to be very consistent. Moreover, the general decrease of
424 Ca concentration in the infected leaves might suggest a compensative mechanism of K to counteract
425 Ca shortage. In fact, it is well known that cations such as K^+ and Na^+ can replace Ca^{2+} in the binding

sites of phosphate and carboxylate groups in cell membranes and cell walls, respectively [39]. Moreover, K^+ leakage from the cytosol to the cell wall is a recognized mechanism connected to the plant response to environmental stresses and pathogens attack leading to metabolic adjustments and even to programmed cell death [52,53]. In this respect, our data achieved *via* synchrotron analysis and showing a greater localization of potassium towards the cell edges of the leaves seems to support this phenomenon also for the ASaV infection. For this reason, K redistribution has been proposed for testing stress-induced injury of plant tissues and a criterion to evaluate the level of stress tolerance [53]. Moreover, the involvement of K in several steps of the translation process including the binding of tRNA to ribosomes [39,54] cannot be excluded in the complex interaction host-pathogen and the infection development, explaining, at least in part, the increase of the nutrient content in particular in the symptomatic areas of the leaf.

In addition to Ca and K, among the macronutrients detected by μ-XRF also P and S are distinguished by changes in their allocation in the infected leaves. In fact, even if the total concentration of these nutrients in the whole leaf did not change because of the viral infection (Fig. 2B and Fig. 2C), marked differences in the spatial distribution appear evident by analysing the maps of the leaves. Indeed, the higher intensity of the fluorescent signal for P and S in the asymptomatic area with respect to the symptomatic one (both belonging to the same infected leaflet) seems to indicate a clear reallocation of the two nutrients towards the healthier zone (Fig. 2A and Fig. 3). In this respect it is interesting to note that an opposite behavior (accumulation of the two nutrients) has been detected in the infected leaf spot of a resilient cultivars of *Vitis vinifera* inoculated with *Plasmopara viticola* [17]. However, it should be highlighted that in the latter case the leaf area infected by the pathogen, due to the expression of resistance traits, underwent rapid necrosis with the death of the involved cells.

P-XRF is characterized by a high limit of quantification for the elements P and S, but also Fe, Mn, Zn and Cu quantification limits are high compared to micronutrients concentrations in flowering ash leaves. Therefore, the following part of the work focused on the set up of an approach for an indirect virus-infection detection based on P-XRF analysis, using exclusively the K and Ca contents (specifically K:Ca ratio) and their fluctuation according to the infection and its levels of development. Our study showed that the leaf K:Ca ratio is clearly modified by the infection of ASaV in flowering ash trees. At the moment, however, the applicability of this approach for the detection of different viral infections of plants or other biotic and abiotic stresses is still to be elucidated. A significant advance towards real in-field applications of these analyses would be the development of an analytical method based on P-XRF allowing an accurate element quantification on fresh leaf samples, being water content still an issue for a correct element quantification. However, if the elements ratio is considered, like in this case, this problem can be less relevant being both elements affected by the

same error. Virus infection could be then confirmed in a lower number of samples by traditional and more specific molecular methods like RT-PCR, thus reducing the costs. These results demonstrate the huge potential of combined XRF techniques to study plants viruses (or more generally plant pathogens) and develop fast diagnostic methods potentially applicable directly in the field.

Conclusions

This study shows how plant viruses can affect the concentration and distribution of micro and macronutrients within the leaf tissue, with certain elements being particularly "sensitive" to such biotic stresses, in particular Ca and K. The combined XRF approach made possible the identification on the one hand of peculiar element distribution patterns in infected symptomatic leaves (*via* μ-XRF) and, on the other hand, the fast determination (*via* P-XRF) of threshold concentration ratios between specific elements (i.e., K and Ca). Results showed how the leaf K:Ca ratio can be modified by ASaV infection in flowering ash trees and how this ratio correlates with the infection status. Statistical analyses showed an accuracy of 86.3% in the classification of healthy and infected leaflets and a 90.0% of accuracy in the identification of infected plants based on K and Ca concentration in leaves. Therefore, K:Ca ratio determined by P-XRF in *Fraxinus ornus* L. leaves appears particularly promising for a rapid, non-destructive and cheap indirect ASaV virus detection to be used alongside the visual evaluation of plant symptoms.

Supplementary material

Table S1: Overview of leaves sampling periods (2019-2021)

Sampled trees (*F. ornus*)	ASaV infection Status	2019 June	2020 August and September	2021 June	2021 July and August
H1	healthy	X	X	X	X
H2	healthy				X
H3	healthy				X
VI1	infected	X	X	X	X
VI2	infected		X	X	X

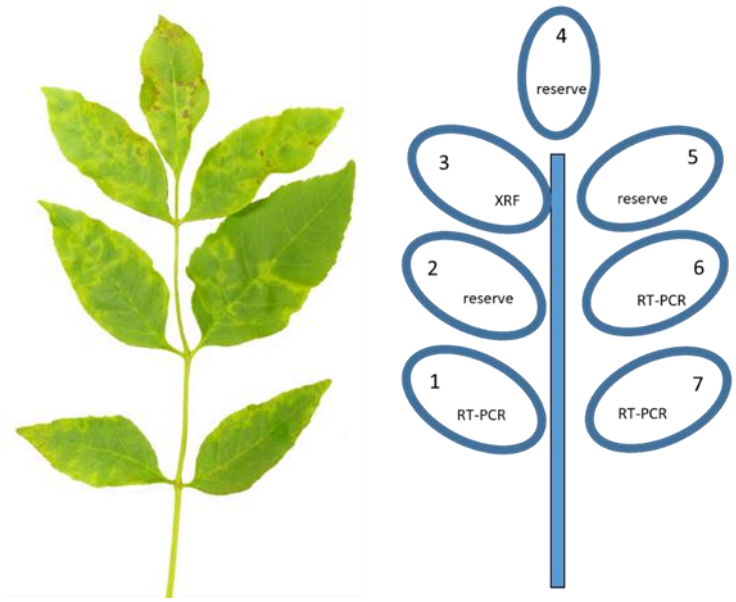

Figure S1: left: ASaV symptomatic leaf and leaflets; right: scheme of leaflets sampling according to analysis

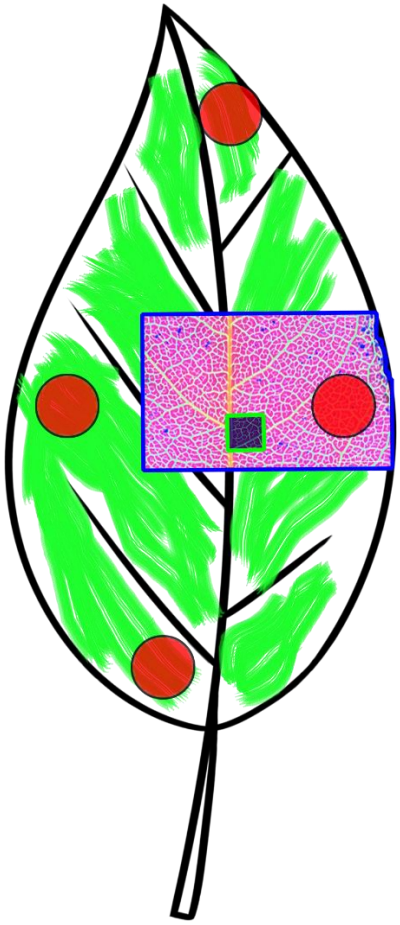

Figure S2: Localisation of the points and areas analysed by the combined XRF methods. Blu rectangle: laboratory μ-XRF mapping area; green square: synchrotron μ-XRF mapping area; red circles: P-XRF points of analysis

Acknowledgements

We acknowledge DESY (Hamburg, Germany), a member of the Helmholtz Association HGF, for the provision of experimental facilities. Parts of this research were carried out at PETRA III and we would like to thank Gianlorenzo Utica and Carlo Fiorini from the Politecnico di Milano (Italy) for giving us the possibility to use the ARDESIA-16 detector and Christina Ossig and Michael Stückelberger from DESY for their help in data elaboration. Laboratory X-ray analyses were performed at the Micro X-ray Lab of the University of Bari "Aldo Moro" (Italy).

Author contributions

Conceptualization: Roberto Terzano, Stefano Cesco, Carlo Porfido, Malgorzata Rybak, Carmen Büttner

Data curation: Carlo Porfido, Ignazio Allegretta, Kira Köpke

Formal analysis: Carlo Porfido, Roberto Terzano, Kira Köpke

Funding acquisition: Carmen Büttner

Investigation: Carlo Porfido, Ignazio Allegretta, Kira Köpke

Methodology: Roberto Terzano, Carlo Porfido, Ignazio Allegretta, Gerald Falkenberg, Kira Köpke, Susanne von Bargen

Project administration: Malgorzata Rybak, Carmen Büttner

Resources: Roberto Terzano, Gerald Falkenberg, Carmen Büttner, Malgorzata Rybak

Software: Carlo Porfido, Ignazio Allegretta, Gerald Falkenberg

Supervision: Roberto Terzano, Stefano Cesco, Tanja Mimmo, Carmen Büttner, Malgorzata Rybak, Susanne von Bargen

Validation: Carlo Porfido, Ignazio Allegretta, Kira Köpke, Martina Bandte

Visualization: Carlo Porfido, Ignazio Allegretta, Kira Köpke

Writing – original draft preparation: Carlo Porfido, Roberto Terzano, Stefano Cesco, Kira Köpke

Writing – review and editing: Tanja Mimmo, Susanne von Bargen, Martina Bandte, Carmen Büttner, Malgorzata Rybak

Carlo Porfido and Kira Köpke contributed equally to this work and should be regarded as joint first authors.

Conflicts of interest

The authors declare no competing interest.

Funding

This work was supported by the Free and Hanseatic City of Hamburg (Germany) - Ministry for Economy and Innovation within the project “Infection of urban trees with pathogens under special consideration of plant viruses - Investigation of street and climate trees in the Hamburg metropolitan region” (project no: 734.650-004/014).

Ignazio Allegretta was supported by a research grant on the project PON R&I “Studio del sistema suolo-pianta mediante tecniche analitiche innovative che impiegano raggi X” – Progetto AIM1809249 – attività 1, linea 1.

Carlo Porfido was supported by a research grant on PRIN 2017 (Progetti di Ricerca di Rilevante Interesse Nazionale)- 2017BHH84R - "Role of Soil- Plant-Microbial Interactions at Rhizosphere Level on the Biogeochemical Cycle and Fate of Contaminants in Agricultural Soils Under Phytoremediation with Biomass Crops (RIZOBIOREM)".

Kira Köpke was supported by the Free and Hanseatic City of Hamburg (Germany) - Ministry for Economy and Innovation within the project “Infection of urban trees with pathogens under special consideration of plant viruses - Investigation of street and climate trees in the Hamburg metropolitan region” (project no: 734.650-004/014).

Data availability

The data supporting the findings of this study are available from the corresponding author (Carlo Porfido), upon request.

References

[1] C. Büttner, S. von Bargen, M. Bandte, H.P. Muehlbach H.P., Forests diseases caused by viruses In: P. Gonthier, G. Nicolotti, Infectious forest diseases, 2013. https://doi.org/10.1079/9781780640402.0000.

[2] M. Bandte, S. von Bargen, M. Landgraf, M. Rybak, C. Büttner. New insights into virus diseases of trees and consequences for tree care. In: Dujesiefken D, eds. Jahrbuch der Baumpflege, Haymarket Media, Braunschweig, (2022) 143-161.

[3] C. Büttner, M. Landgraf, H. Fernandez Colino, S. von Bargen, M. Bandte. Virus diseases of forest and urban trees. In: Asiegbu F, Kovalchuk A, eds. Forest Microbiology. Tree diseases and pests 3, 61-97 (2022).

[4] S. Massart, A. Olmos, H. Jijakli, T. Candresse, Current impact and future directions of high throughput sequencing in plant virus diagnostics, Virus Res. 188 (2014). https://doi.org/10.1016/j.virusres.2014.03.029.

[5] S. Massart, T. Candresse, J. Gil, C. Lacomme, L. Predajna, M. Ravnikar, J.S. Reynard, A. Rumbou, P. Saldarelli, D. Škoric, E.J. Vainio, J.P.T. Valkonen, H. Vanderschuren, C. Varveri, T. Wetzel, A framework for the evaluation of biosecurity, commercial, regulatory, and scientific impacts of plant viruses and viroids identified by NGS technologies, Front. Microbiol. 8 (2017). https://doi.org/10.3389/fmicb.2017.00045.

[6] Correction: A novel badnavirus discovered from Betula sp. affected by birch leaf-roll disease (PLoS ONE (2018) 13: 3 (e0193888) DOI: 10.1371/journal.pone.0193888), PLoS One. 13 (2018). https://doi.org/10.1371/journal.pone.0200555.

[7] S. von Bargen, R. Al Kubrusli, T. Gaskin, S. Fürl, F. Hüttner, D.R. Blystad, D.G. Karlin, R. Jalkanen, C. Büttner, Characterisation of a novel Emaravirus identified in mosaic-diseased Eurasian aspen (Populus tremula), Ann. Appl. Biol. 176 (2020). https://doi.org/10.1111/aab.12576.

576 [8] M. Bandte, M. Rehanek, B. Leder, S. von Bargen, C. Büttner, Identification of an emaravirus
577 in a common oak (Quercus robur l.) conservation seed orchard in germany: Implications for oak
578 health, Forests. 11 (2020) 1–14. https://doi.org/10.3390/f11111174.
579 [9] M. Rehanek, S. von Bargen, M. Bandte, D.G. Karlin, C. Büttner, A novel emaravirus
580 comprising five RNA segments is associated with ringspot disease in oak, Arch. Virol. 166 (2021).
581 https://doi.org/10.1007/s00705-021-04955-w.
582 [10] A. Rumbou, T. Candresse, S. von Bargen, C. Büttner, Next-Generation Sequencing Reveals
583 a Novel Emaravirus in Diseased Maple Trees From a German Urban Forest, Front. Microbiol. 11
584 (2021). https://doi.org/10.3389/fmicb.2020.621179.
585 [11] A. Rumbou, E.J. Vainio, C. Büttner, Towards the forest virome: High-throughput sequencing
586 drastically expands our understanding on virosphere in temperate forest ecosystems, Microorganisms.
587 9 (2021). https://doi.org/10.3390/microorganisms9081730.
588 [12] E. Bright Opoku, M. Landgraf, K. Pack, M. Bandte, S. von Bargen, M. Schreiner, B. Jackel,
589 C. Buttner, Emerging Plant Viruses in Urban Green: Detection of the Virome in Birch (Betula sp.),
590 J. Hortic. 05 (2018). https://doi.org/10.4172/2376-0354.1000233.
591 [13] A. Rumbou, T. Candresse, A. Marais, L. Svanella-Dumas, M. Landgraf, S. von Bargen, C.
592 Büttner, Unravelling the virome in birch: RNA-Seq reveals a complex of known and novel viruses,
593 PLoS One. 15 (2020). https://doi.org/10.1371/journal.pone.0221834.
594 [14] G. D'attoma, M. Morelli, P. Saldarelli, M. Saponari, A. Giampetruzzi, D. Boscia, V.N.
595 Savino, L.D. La Fuente, P.A. Cobine, Ionomic differences between susceptible and resistant olive
596 cultivars infected by Xylella fastidiosa in the outbreak area of salento, Italy, Pathogens. 8 (2019).
597 https://doi.org/10.3390/pathogens8040272.
598 [15] S. Ali, A. Tyagi, H. Bae, Ionomic approaches for discovery of novel stress-resilient genes in
599 plants, Int. J. Mol. Sci. 22 (2021). https://doi.org/10.3390/ijms22137182.
600 [16] K. Hančević, T. Radić, I. Pasković, B. Urlić, Biochemical and physiological responses to long-
601 term Citrus tristeza virus infection in Mexican lime plants, Plant Pathol. 67 (2018).
602 https://doi.org/10.1111/ppa.12799.
603 [17] S. Cesco, A. Tolotti, S. Nadalini, S. Rizzi, F. Valentinuzzi, T. Mimmo, C. Porfido, I.
604 Allegretta, O. Giovannini, M. Perazzolli, G. Cipriani, R. Terzano, I. Pertot, Y. Pii, Plasmopara viticola
605 infection affects mineral elements allocation and distribution in Vitis vinifera leaves, Sci. Rep. 10
606 (2020). https://doi.org/10.1038/s41598-020-75990-x.
607 [18] N. Yardimci, H. Eryigit, I. Erdal. Effect of alfalfa mosaic virus (AM) on the content of some
608 macro- and micronutrients in alfalfa. Journal of culture collections 5, 90-93 (2007).

609 [19] U. Panne, Environmental Analytical Chemistry. 2nd Edition. Edited by F. W. Fifield and P.
610 J. Haines, Angew. Chemie Int. Ed. 40 (2001). https://doi.org/10.1002/1521-
611 3773(20010917)40:18<3480::aid-anie11113480>3.0.co;2-y.
612 [20] E. Marguí, I. Queralt, M. Hidalgo, Application of X-ray fluorescence spectrometry to
613 determination and quantitation of metals in vegetal material, TrAC - Trends Anal. Chem. 28 (2009)
614 362–372. https://doi.org/10.1016/j.trac.2008.11.011.
615 [21] G.G. Arantes De Carvalho, M.B. Bueno Guerra, A. Adame, C.S. Nomura, P.V. Oliveira, H.W.
616 Pereira De Carvalho, D. Santos, L.C. Nunes, F.J. Krug, Recent advances in LIBS and XRF for the
617 analysis of plants, J. Anal. At. Spectrom. 33 (2018) 919–944. https://doi.org/10.1039/c7ja00293a.
618 [22] R. Terzano, M.A. Denecke, G. Falkenberg, B. Miller, D. Paterson, K. Janssens, Recent
619 advances in analysis of trace elements in environmental samples by X-ray based techniques (IUPAC
620 Technical Report), Pure Appl. Chem. 91 (2019). https://doi.org/10.1515/pac-2018-0605.
621 [23] A. Turner, C.C. Chan, M.T. Brown, Application of field-portable-XRF for the determination
622 of trace elements in deciduous leaves from a mine-impacted region, Chemosphere. 209 (2018) 928–
623 934. https://doi.org/10.1016/j.chemosphere.2018.06.110.
624 [24] R. Terzano, M. Alfeld, K. Janssens, B. Vekemans, T. Schoonjans, L. Vincze, N. Tomasi, R.
625 Pinton, S. Cesco, Spatially resolved (semi)quantitative determination of iron (Fe) in plants by means
626 of synchrotron micro X-ray fluorescence, Anal. Bioanal. Chem. 405 (2013).
627 https://doi.org/10.1007/s00216-013-6768-6.
628 [25] F. Valentinuzzi, Y. Pii, P. Carlo, T. Roberto, M.C. Fontanella, G.M. Beone, S. Astolfi, T.
629 Mimmo, S. Cesco, Root-shoot-root Fe translocation in cucumber plants grown in a heterogeneous Fe
630 provision, Plant Sci. 293 (2020). https://doi.org/10.1016/j.plantsci.2020.110431.
631 [26] S.M. Brouwer, P. Lindqvist-Reis, D.P. Persson, S. Marttila, L.J. Grenville-Briggs, E.
632 Andreasson, Visualising the ionome in resistant and susceptible plant–pathogen interactions, Plant J.
633 108 (2021) 870–885. https://doi.org/10.1111/tpj.15469.
634 [27] F. Naim, K. Khambatta, L.M.V.P. Sanglard, G. Sauzier, J. Reinhardt, D.J. Paterson, A.
635 Zerihun, M.J. Hackett, M.R. Gibberd, Synchrotron X-ray fluorescence microscopy-enabled elemental
636 mapping illuminates the “battle for nutrients” between plant and pathogen, J. Exp. Bot. 72 (2021)
637 2757–2768. https://doi.org/10.1093/jxb/erab005.
638 [28] Schönfeld P. 2019. “Klimabäume” - Welche Arten können in Zukunft gepflanzt werden?
639 LWGaktuell. Bayerische Landesanstalt für Weinbau und Gartenbau, Institut für Stadtgrün und
640 Landschaftsbau, Veitshöchheim. https://www.lwg.bayern.de/mam/cms0
641 6/landespflege/dateien/zukunft_klimabaeume.pdf. Accessed September 2022.

642 [29] Deutsche Gartenamtsleiterkonferenz. 2020. Zukunftsbäume für Die Stadt Auswahl aus der
643 GALK-Strassenbaumliste. https://www.galk.de/component/jdownloads/send/4-
644 informationsflyer/664-broschuere-zukunftsbaeume-galk-und-bdb-2020 . Accessed September 2022.
645 [30] T.R. Gaskin, M. Tischendorf, I. Günther, M. Rehanek, C. Büttner, S. von Bargen,
646 Characterization of a novel emaravirus affecting ash species (Fraxinus spp.) in europe, Forests. 12
647 (2021) 1–21. https://doi.org/10.3390/f12111574.
648 [31] D. Kasang. Klimaänderungen in Hamburg. https://bildungsserver.hamburg.de/regionale-
649 klimaaenderungen/2933364/hamburg/. Accessed September 2022.
650 [32] H. von Storch, M. Claussen. Klimabericht für die Metropolregion Hamburg. Springer (2010).
651 [33] Deutscher Wetterdienst. Hamburg (Flugh.)
652 https://www.dwd.de/DE/wetter/wetterundklima_vorort/schleswig-
653 holstein_hamburg/hamburg/_node.html. Accessed September 2022.
654 [34] Deutscher Wetterdienst. Klimadaten Deutschland - Monats- und Tageswerte (Archiv)
655 Hamburg-Fühlsbüttel.
656 https://www.dwd.de/DE/leistungen/klimadatendeutschland/klarchivtagmonat.html?nn=16102
657 Accessed September 2022.
658 [35] USS Working Group WRB. 2015. World Reference Base for Soil Resources 2014, update
659 2015. International soil classification system for naming soils and creating legends for soil maps.
660 World Soil Resources Reports No. 106. FAO, Rome.
661 [36] V.A. Solé, E. Papillon, M. Cotte, P. Walter, J. Susini, A multiplatform code for the analysis
662 of energy-dispersive X-ray fluorescence spectra, Spectrochim. Acta Part B At. Spectrosc. 62 (2007)
663 63–68. https://doi.org/10.1016/j.sab.2006.12.002.
664 [37] M. Alfeld, K. Janssens, Strategies for processing mega-pixel X-ray fluorescence hyperspectral
665 data: A case study on a version of Caravaggio's painting Supper at Emmaus, J. Anal. At. Spectrom.
666 (2015). https://doi.org/10.1039/c4ja00387j.
667 [38] G. Utica, E. Fabbrica, M. Carminati, G. Borghi, N. Zorzi, F. Ficorella, A. Picciotto, I.
668 Allegretta, G. Falkenberg, C. Fiorini, ARDESIA-16: A 16-channel SDD-based spectrometer for
669 energy dispersive X-ray fluorescence spectroscopy, J. Instrum. 16 (2021).
670 https://doi.org/10.1088/1748-0221/16/07/P07057.
671 [39] P. Marschner, Marschner's Mineral Nutrition of Higher Plants: Third Edition, 2011.
672 https://doi.org/10.1016/C2009-0-63043-9.
673 [40] P.J. White, M.R. Broadley, Calcium in plants, Ann. Bot. 92 (2003) 487–511.
674 https://doi.org/10.1093/aob/mcg164.

675 [41] M. Gilliham, M. Dayod, B.J. Hocking, B. Xu, S.J. Conn, B.N. Kaiser, R.A. Leigh, S.D.
676 Tyerman, Calcium delivery and storage in plant leaves: Exploring the link with water flow, J. Exp.
677 Bot. 62 (2011) 2233–2250. https://doi.org/10.1093/jxb/err111.
678 [42] W. Fricke, P.S. Hinde, R.A. Leigh, A.D. Tomos, Vacuolar solutes in the upper epidermis of
679 barley leaves: Intercellular differences follow patterns, Planta An Int. J. Plant Biol. 196 (1995).
680 https://doi.org/10.1007/BF00193215.
681 [43] M. Kerton, H.J. Newbury, D. Hand, J. Pritchard, Accumulation of calcium in the centre of
682 leaves of coriander (Coriandrum sativum L.) is due to an uncoupling of water and ion transport, J.
683 Exp. Bot. 60 (2009) 227–235. https://doi.org/10.1093/jxb/ern279.
684 [44] W.J. Conradie, Seasonal Uptake of Nutrients by Chenin Blanc in Sand Culture: II.
685 Phosphorus, Potassium, Calcium and Magnesium, South African J. Enol. Vitic. 2 (2017).
686 https://doi.org/10.21548/2-1-2403.
687 [45] G.G. Erion, W.E. Riedell, Barley yellow dwarf virus effects on cereal plant growth and
688 transpiration, Crop Sci. 52 (2012) 2794–2799. https://doi.org/10.2135/cropsci2012.02.0138.
689 [46] R.R. Murray, M.S.M. Emblow, A.M. Hetherington, G.D. Foster, Plant virus infections control
690 stomatal development, Sci. Rep. 6 (2016) 1–7. https://doi.org/10.1038/srep34507.
691 [47] Y. Yang, J. Shah, D.F. Klessig, Signal perception and transduction in plant defense responses,
692 Genes Dev. 11 (1997). https://doi.org/10.1101/gad.11.13.1621.
693 [48] D. Scheel, Resistance response physiology and signal transduction, Curr. Opin. Plant Biol. 1
694 (1998). https://doi.org/10.1016/1369-5266(88)80051-7.
695 [49] J. Foreman, V. Demidchik, J.H.F. Bothwell, P. Mylona, H. Miedema, M. Angel Torres, P.
696 Linstead, S. Costa, C. Brownlee, J.D.G. Jones, J.M. Davies, L. Dolan, Reactive oxygen species
697 produced by NADPH oxidase regulate plant cell growth, Nature. 422 (2003).
698 https://doi.org/10.1038/nature01485.
699 [50] A. Amtmann, S. Troufflard, P. Armengaud, The effect of potassium nutrition on pest and
700 disease resistance in plants, in: Physiol. Plant., 2008. https://doi.org/10.1111/j.1399-
701 3054.2008.01075.x.
702 [51] X. Jing, X. Song, S. Cai, P. Wang, G. Lu, L. Yu, C. Zhang, Z. Wu, Overexpression of
703 OsHAK5 potassium transporter enhances virus resistance in rice (Oryza sativa), Mol. Plant Pathol.
704 23 (2022). https://doi.org/10.1111/mpp.13211.
705 [52] V. Demidchik, D. Straltsova, S.S. Medvedev, G.A. Pozhvanov, A. Sokolik, V. Yurin, Stress-
706 induced electrolyte leakage: The role of K+-permeable channels and involvement in programmed cell
707 death and metabolic adjustment, J. Exp. Bot. 65 (2014) 1259–1270.
708 https://doi.org/10.1093/jxb/eru004.

[53] K. Vogel-Mikuš, P. Pongrac. Imaging of Potassium and Calcium Distribution in Plant Tissues and Cells to Monitor Stress Response and Programmed Cell Death. In: M. Klemenčič, S. Stael, P.F. Huesgen, eds. Plant Proteases and Plant Cell Death: Methods and Protocols, Methods in Molecular Biology, 2447, (2022) 233-246.

[54] R.G. Wyn Jones, C.J. Brady, J. Spiers. Ionic and osmotic relations in plant cells. In: Adran Biocemeg a Gwyddor Pridd, Coleg Prifysgol Gogledd Cymru, Bangor, Gwynedd, Wales, CSIRO, Division of Food Research, Plant Physiology Unit, School of Biological Sciences, Macquarie University, Sydney, NSW., eds. Recent advances in cereal biochemistry, (1979) 63-103.